



Label-free sensing of cells with fluorescence lifetime imaging: The quest for metabolic heterogeneity

Evgeny A. Shirshin^a, Marina V. Shirmanova^b, Alexey V. Gayer^a, Maria M. Lukina^b, Elena E. Nikonova^a, Boris P. Yakimov^a, Gleb S. Budylin^a, Varvara V. Dudenkova^b, Nadezhda I. Ignatova^b, Dmitry V. Komarov^c, Vladislav V. Yakovlev^{d,1} , Wolfgang Becker^e, Elena V. Zagaynova^b, Vladislav I. Shcheslavskiy^{b,e}, and Marlan O. Scully^{d,f,1}

^aFaculty of Physics, M. V. Lomonosov Moscow State University, 119991 Moscow, Russia; ^bInstitute of Experimental Oncology and Biomedical Technologies, Privolzhsky Research Medical University, 603005 Nizhny Novgorod, Russia; ^cVolga District Medical Center, 603001 Nizhny Novgorod, Russia; ^dInstitute for Quantum Science and Engineering, Texas A&M University, College Station, TX 77843; ^eBecker & Hickl GmbH, 12277 Berlin, Germany; and ^fDepartment of Physics, Baylor University, Waco, TX 76798

Contributed by Marlan O. Scully; received October 21, 2021; accepted January 14, 2022; reviewed by Vanderlei Bagnato and Ammasi Periasamy

Molecular, morphological, and physiological heterogeneity is the inherent property of cells which governs differences in their response to external influence. Tumor cell metabolic heterogeneity is of a special interest due to its clinical relevance to tumor progression and therapeutic outcomes. Rapid, sensitive, and non-invasive assessment of metabolic heterogeneity of cells is a great demand for biomedical sciences. Fluorescence lifetime imaging (FLIM), which is an all-optical technique, is an emerging tool for sensing and quantifying cellular metabolism by measuring fluorescence decay parameters of endogenous fluorophores, such as NAD(P)H. To achieve accurate discrimination between metabolically diverse cellular subpopulations, appropriate approaches to FLIM data collection and analysis are needed. In this paper, the unique capability of FLIM to attain the overarching goal of discriminating metabolic heterogeneity is demonstrated. This has been achieved using an approach to data analysis based on the non-parametric analysis, which revealed a much better sensitivity to the presence of metabolically distinct subpopulations compared to more traditional approaches of FLIM measurements and analysis. The approach was further validated for imaging cultured cancer cells treated with chemotherapy. These results pave the way for accurate detection and quantification of cellular metabolic heterogeneity using FLIM, which will be valuable for assessing therapeutic vulnerabilities and predicting clinical outcomes.

fluorescence lifetime | cancer | heterogeneity | imaging | metabolism

Solid tumors are complex systems characterized by spatial heterogeneity at the genetic, molecular, and cellular levels. Tumor heterogeneity is the critical phenomenon determining the difference in therapeutic outcomes for patients with similar histological diagnosis (1, 2). The development of omics technologies allowed for a detailed investigation of molecular pathways responsible for tumor heterogeneity, which is now considered to be a prerequisite for fast tumor growth rather than just a consequence of the neoplastic transformation and multiple mutations. Metabolic heterogeneity, i.e., the difference in cancer cell metabolism within a tumor and between tumors, is considered to be a negative prognostic factor and is accompanied by an increased probability of recurrence and higher mortality (3). The basis of metabolic heterogeneity is the ability of cancer cells to adapt to nonuniform microenvironment, e.g., local hypoxia and nutrient limitation (2), and some factors intrinsic to the cancer cells, e.g., differentiation state, proliferative activity, and genetic alterations (4).

Cancer cells are capable of switching between different metabolic pathways (e.g., aerobic glycolysis and oxidative phosphorylation) depending on the local conditions. This phenomenon is known as metabolic plasticity (5). Therefore, the metabolic status may be highly variable for the cells within a single tumor and between different tumors of the same type (6–9). Evidently, visualization and quantification of metabolic heterogeneity could be helpful for optimization of cancer treatment. Hence, methods

allowing for rapid, sensitive, and noninvasive assessment of cellular metabolic heterogeneity are a high demand for oncology.

During the last decade, fluorescence lifetime imaging (FLIM) (10), which is an all-optical technique, has proven to be a useful tool to characterize cellular metabolic state on a label-free basis. Metabolic imaging by FLIM is based on measuring fluorescence decay parameters (FDPs) of endogenous fluorophores, such as reduced nicotinamide adenine dinucleotide (phosphate) NAD(P)H and oxidized flavin adenine dinucleotide, FAD, which are involved in a number of redox reactions within the cell. It is now established that FLIM is sensitive to alterations in energy metabolism accompanying carcinogenesis (11) and cancer cell response to therapies and that it correlates with standard biochemical and molecular assays (12–14). It was shown that FLIM enables visualization of cellular metabolic heterogeneity of cancer, both intrinsic and induced by anticancer therapy (15–22). However, a detailed performance comparison of different FLIM data analysis methods in quantification of metabolic heterogeneity (variability) in populations of cells has not been considered.

Significance

Tumors are complex systems characterized by spatial heterogeneity at the genetic, molecular, and cellular levels. Tumor heterogeneity is the critical phenomenon determining the difference in therapeutic outcomes for patients with similar histological diagnosis. Metabolic heterogeneity, i.e., the difference in cancer cell metabolism within a tumor and between tumors, is considered to be a negative prognostic factor and is accompanied by an increased probability of recurrence and higher mortality. Detection and quantification of metabolic heterogeneity can help in diagnosing cancer, assessing tumor progression, and optimizing cancer treatment. Here, we demonstrate that fluorescence lifetime imaging with the advanced detection and signal analysis system may allow rapid, sensitive, and noninvasive assessment of cellular metabolic heterogeneity in living cells.

Author contributions: E.A.S., M.V.S., E.E.N., B.P.Y., V.V.Y., V.I.S., and M.O.S. designed research; E.A.S., M.V.S., A.V.G., M.M.L., E.E.N., B.P.Y., G.S.B., V.V.D., N.I.I., D.V.K., E.V.Z., and V.I.S. performed research; M.V.S., M.M.L., G.S.B., V.V.D., N.I.I., D.V.K., W.B., E.V.Z., and V.I.S. contributed new reagents/analytic tools; E.A.S., M.V.S., A.V.G., M.M.L., E.E.N., B.P.Y., G.S.B., V.V.Y., W.B., V.I.S., and M.O.S. analyzed data; and E.A.S., M.V.S., V.V.Y., V.I.S., and M.O.S. wrote the paper.

Reviewers: V.B., Universidade de São Paulo; and A.P., University of Virginia.

The authors declare no competing interest.

This article is distributed under [Creative Commons Attribution-NonCommercial-NoDerivatives License 4.0 \(CC BY-NC-ND\)](https://creativecommons.org/licenses/by-nc-nd/4.0/).

¹To whom correspondence may be addressed. Email: yakovlev@tamu.edu or scully@tamu.edu.

This article contains supporting information online at <http://www.pnas.org/lookup/suppl/doi:10.1073/pnas.2118241119/-DCSupplemental>.

Published February 25, 2022.

The FLIM-based assessment of metabolic heterogeneity at the cellular level can be reduced to the problem of discrimination between several subpopulations of cells which differ in their FDPs. Therefore, it is important to find a way that provides the highest sensitivity to discriminate between metabolically different subpopulations of cells. First, the FLIM image can be analyzed as a whole, and, consequently, the overall distribution of FDPs is analyzed over all pixels of the image. Another option is the segmentation of the image into individual objects (single cells, organelles, etc.), calculation of FDPs for each object, and analysis of the FDP distribution for the segmented objects. Both approaches are used in the literature, but there is a general understanding that the latter is more sensitive to the presence of cell subpopulations different in their metabolism (21–23). Second, the FLIM data can be processed either parametrically, i.e., by fitting the decay curves to a model [e.g., biexponential decay in the case of NAD(P)H and FAD] or nonparametrically. The latter approach includes the analysis of phasor plots (24, 25) or using different clustering algorithms (26), Bayesian frameworks (27, 28), and deep neural networks (29). Nonparametric methods of FLIM data analysis are extensively used due to the simplicity of interpretation of the results and the lack of necessity for data fitting, which may require calculation time. The workflow for the assessment of cancer cell metabolic heterogeneity using clustering of FDPs is schematically presented in Fig. 1.

In this paper, we present the results of assessment of cancer cell metabolic heterogeneity on the basis of FLIM of NAD(P)H for the simulated and experimental data using parametric (fitting to biexponential decay model) and nonparametric (phasor plot and K-means clustering) methods. By calculating the dimensionless bimodality index (BI), which characterizes the presence of two clusters of cells, we aimed at a quantitative comparison between the sensitivity of different approaches to FLIM data analysis in search of metabolic heterogeneity. To support the numerical simulation results, the metabolic heterogeneity was assessed in a colorectal cancer cell line and in primary cell cultures derived from patients' colorectal tumor upon chemotherapy. The obtained results pave the way for a more

precise detection and quantification of cellular metabolic heterogeneity using FLIM.

Results

Analysis of Bimodality in the FLIM Data: Numerical Simulation. To assess the performance of different FLIM data analysis methods for characterization of metabolic heterogeneity, we considered the simplest yet realistic model: the system containing two clusters of cells, each characterized by a different set of FDPs. The presence of two subpopulations of cells should lead to bimodality of FDP distribution—for instance, in the mean fluorescence lifetime distribution two peaks should be observed. However, broadening of distributions caused by dispersion of FDPs may result in the absence of visible bimodality.

The width of the distribution of the fluorescence lifetime (or other FDPs) is determined by three factors:

- 1) intracellular dispersion σ_{intra} , which originates from the heterogeneity of the cell's structure and nonuniform fluorescence lifetime distribution within the cell,
- 2) intercellular dispersion σ_{inter} , which originates from heterogeneous distribution of fluorescence lifetime over individual cells within the system, and
- 3) dispersion σ_{fit} , which originates from the error of fluorescence decay approximation.

These three dispersions contribute to the overall width of the FDP distribution obtained either for the whole image (i.e., distribution over binned pixels) or segmented cells (i.e., distribution over individual cells). However, the impact of σ_{intra} , σ_{inter} , and σ_{fit} on the width of the fluorescence lifetime distribution is different for the whole image and segmented cell analysis. Intracellular dispersion, σ_{intra} , is lower in the latter case: Each cell is characterized by a fluorescence decay curve obtained by averaging over all pixels within this cell, which reduces the dispersion of FDPs caused by cellular heterogeneity. The fitting error σ_{fit} depends on the number of photons under the fluorescence decay curve N roughly as $\sim \frac{1}{\sqrt{N}}$; hence, it is lower when the signal is averaged over the whole cell.

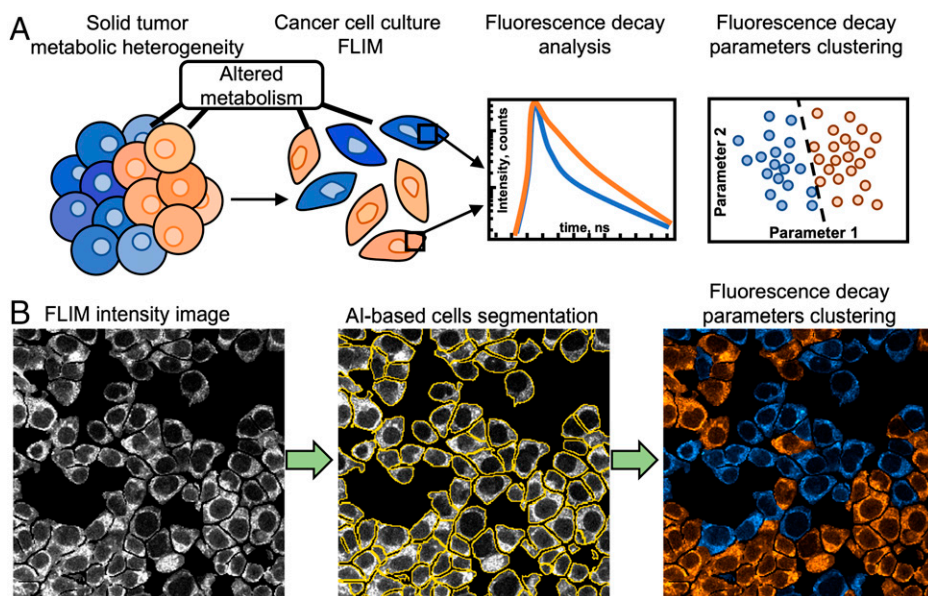


Fig. 1. Illustration of tumor metabolic heterogeneity evaluation using FLIM. (A) Cancer cells are examined using metabolic FLIM, which provides the kinetics of fluorescence decay from each pixel of the image. The obtained fluorescence decay signal depends on the metabolic state of the cell and can further be analyzed using various parametric and nonparametric methods, which can accurately predict metabolically distinct subpopulations. (B) Automatic segmentation of cells in FLIM images using artificial intelligence (AI)-based approaches allows for the assessment of metabolic heterogeneity on a single cell level.

Intercellular dispersion of FDPs σ_{inter} does not depend on the method of analysis. Hence, it can be suggested that the fluorescence lifetime distribution would be narrower in the case of the analysis for individual cells, thus resulting in a better discrimination between the subpopulations.

To verify this hypothesis, numerical simulation of the FLIM data was performed as described in *Materials and Methods*. Intercellular and intracellular dispersions were taken as $\sigma_{intra} = \sigma_{inter} \approx 100$ ps, corresponding to typical experimentally determined parameters for NAD(P)H fluorescence (see *SI Appendix, Table S1* and the references therein), and the width of the instrument response function (IRF) was set to 100 ps. Representative simulated fluorescence decay curves are shown in *SI Appendix, Fig. S1*.

The numerical simulations were performed for different ratios of cells number in two clusters $\pi = \frac{N_1}{N_1 + N_2}$ (also referred as to “Cluster 1, %”), where N_1 and N_2 are the numbers of cells in subpopulations, and for different values of $\Delta\tau_{mean}$, which is the distance between the median mean fluorescence lifetimes in subpopulations. The value of π varied in the 50 to 90% range, and $\Delta\tau_{mean}$ varied from 50 to 400 ps. As a measure of bimodality, the BI (30) and its modifications for different FLIM processing methods were used (see *Materials and Methods* for details). The threshold corresponding to the presence of bimodality in the distribution was set to $BI > 1.1$ (30), while the statistical significance of the obtained BI values is calculated within the assumption that data are not bimodal, i.e., low P value suggests the presence of the bimodality in data (the evaluation of the statistical significance of the BI is described in *SI Appendix, Fig. S2*).

We applied three approaches for FLIM data processing: fitting to a biexponential decay model (Fig. 2A), phasor plot analysis (Fig. 2B), and clustering of the fluorescence decay curves (Fig. 2C).

In each case, a hypothesis about the presence of two modes was tested, namely 1) distribution of the mean fluorescence lifetime was fitted to two Gaussians, 2) the density of phasor plot population was fitted to a sum of two two-dimensional Gaussians, and 3) the set of fluorescence decay curves obtained for all cells was clustered into two subsets using the K-means algorithm. Next, for each of two modes the median values μ and SDs σ were obtained and, based on them, the BI was calculated. The representative results of bimodality assessment using all three methods are demonstrated in Fig. 2 D–F and in *SI Appendix, Figs. S3–S5* for a broad range of $\Delta\tau_{mean}$ and π . At high $\Delta\tau_{mean}$ values (~ 350 ps), i.e., when the difference of FDPs in two clusters of cells is large, two modes are clearly seen in the data (Fig. 2 D–F, panels in a green frame). However, upon the decrease in $\Delta\tau_{mean}$, the modes corresponding to two subpopulations are superimposed, and the BI becomes low ($BI < 1.1$, bimodality not detected, red frame in Fig. 2 D–F). Using the described approach, we performed comparison of three methods of FLIM data processing performance in the assessment of bimodality. Moreover, the analyses over the whole image and segmented cells were compared.

As a metrics performance, we have calculated the fraction of cells Cluster 1 correctly attributed to the Cluster 1 by the algorithm: For the modeled data, this information is known a priori. The fraction of cells correctly assigned to Cluster 1 (with lower τ_{mean} ; see *Cluster Performance Evaluation*) was plotted for multiple cases with different ratio of cells truly belonging to Cluster 1 $\pi = N_1/(N_1 + N_2) = 90, 70,$ and 50% as a function of $\Delta\tau_{mean}$ (Fig. 3).

First, it can be clearly seen that the analysis over segmented cells always outperforms the analysis over the whole image (Fig. 3A). This observation agrees with the hypothesis that a decrease in intracellular dispersion σ_{intra} and fitting error σ_{fit} in

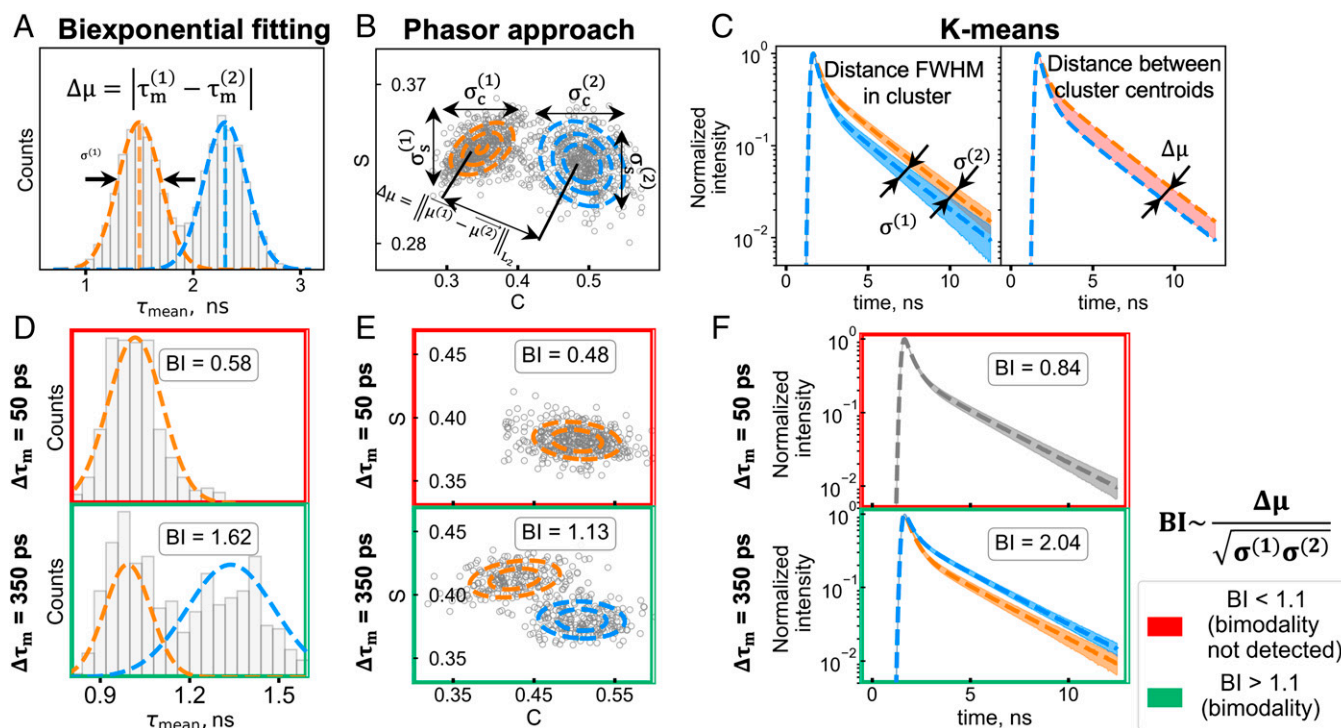


Fig. 2. Schematic representation of bimodality assessment using (A) the distribution of mean fluorescence lifetime, (B) population density of phasor plot, and (C) K-means clustering of fluorescence decay curves. The data were obtained using numerical simulation. Under the assumption of the presence of two subpopulations, two modes are detected for each method of FLIM data analysis, and then the median value (μ) and SD (σ) for each mode are used to calculate the BI. The results of bimodality assessment for two values of $\Delta\tau_{mean}$ (50 and 350 ps) using the BI estimation from (D) the distribution of mean fluorescence lifetime, (E) population density of phasor plot, and (F) K-means clustering of fluorescence decay curves. The analysis was performed over segmented cells.

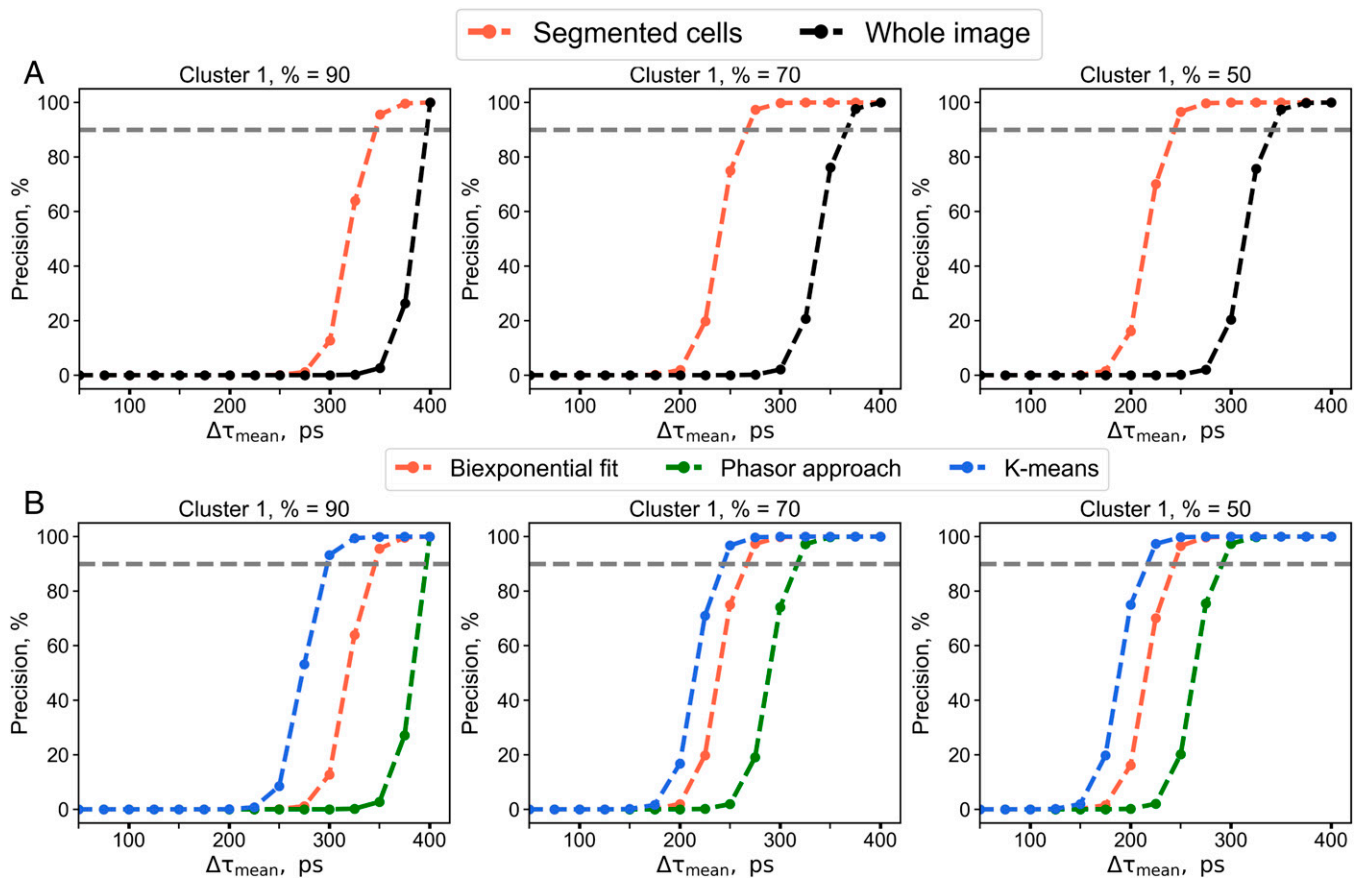


Fig. 3. (A) The dependence of the fraction of cells correctly attributed to its cluster on the distance between the median fluorescence lifetimes in the clusters ($\Delta\tau_{mean}$) obtained using biexponential fitting for whole-image analysis (red) and for segmented cells (black). (B) The dependence of the fraction of cells correctly attributed to its cluster on the distance between the median fluorescence lifetimes in the clusters ($\Delta\tau_{mean}$) obtained using biexponential fitting (red), phasor plot analysis (green), and K-means clustering (blue). The gray horizontal line corresponds to precision of 90% in attribution of cells to the correct cluster. The dependencies presented in A and B were calculated for fraction of cells belonging to Cluster 1 equal to 90%, 70%, and 50%.

the case of segmented cell analysis results in a better capability to detect the presence of two cell clusters in the system. We also note that in the case of the bin size equal to or exceeding the cell size the fitting error would decrease; however, such binning values result in artifacts connected with mixing the signals from neighboring cells or between the cells and intercellular space. Thus, increasing the size of the bin when processing the FLIM data does not allow for better detection of cells metabolic heterogeneity (see *SI Appendix*, Fig. S6).

Second, the results of the numerical simulation show that at high values of $\Delta\tau_{mean}$ (~ 300 ps) all three methods of FLIM data analysis demonstrate similar performance (Fig. 3B). However, the K-means clustering exhibits the best performance compared to other methods for all of the considered fractions of the cells (Cluster 1, %) and correctly identifies the cluster to which the cell belongs at the lowest $\Delta\tau_{mean}$ compared to other methods (Fig. 3B). The possibility to separate the clusters that have small differences in fluorescence lifetime parameters with high accuracy is very important when analyzing metabolic heterogeneity by NAD(P)H fluorescence lifetime (*SI Appendix*, Table S2). Our results clearly show the importance of cell segmentation for the detection of subpopulations of cells and underline the advantages of nonparametric methods, namely K-means, clustering.

Automatic Segmentation Algorithm. For the further analysis of the FDPs of single cells on the experimentally obtained FLIM images, automatic segmentation algorithms were applied. Automatic segmentation of cells is necessary both for obtaining

appropriate statistics ($\sim 1,000$ cells) for metabolic heterogeneity assessment in cellular populations and for creation of a rapid clinical test free of manual image analysis. To find cell borders and nuclei and segment cultured cells in FLIM images, we used the deep-learning approach based on the U-Net neural network (31) trained on the manually segmented images of the HCT116 colorectal cancer cell line with additional postprocessing of image borders to obtain single cells. Overall, the developed approach allowed us to analyze the information from 89% of single cells presented in the FLIM images of HCT116 cell lines (total amount of cells = 749) and 94% of cells in manually segmented regions of the intensity images of the patient-derived cancer cells (total amount of cells = 768). More details on the developed segmentation approach are presented in *Materials and Methods* and *SI Appendix*.

Analysis of Bimodality in the FLIM Data: Experimental Studies. To support the results of numerical simulations, FLIM measurements of NAD(P)H were performed for the live cultured colorectal cancer cells. In the first series of experiments, we used the human colorectal carcinoma cell line HCT116 treated for 24 h with different doses of 5-fluorouracil (5-FU), a standard chemotherapeutic agent (32).

The example in Fig. 4 demonstrates that chemotherapy with 5-FU induced heterogeneous response in terms of cellular metabolism within the population of cultured cancer cells. Given the performance of different methods (Fig. 3), the analysis was performed using the mean fluorescence lifetime

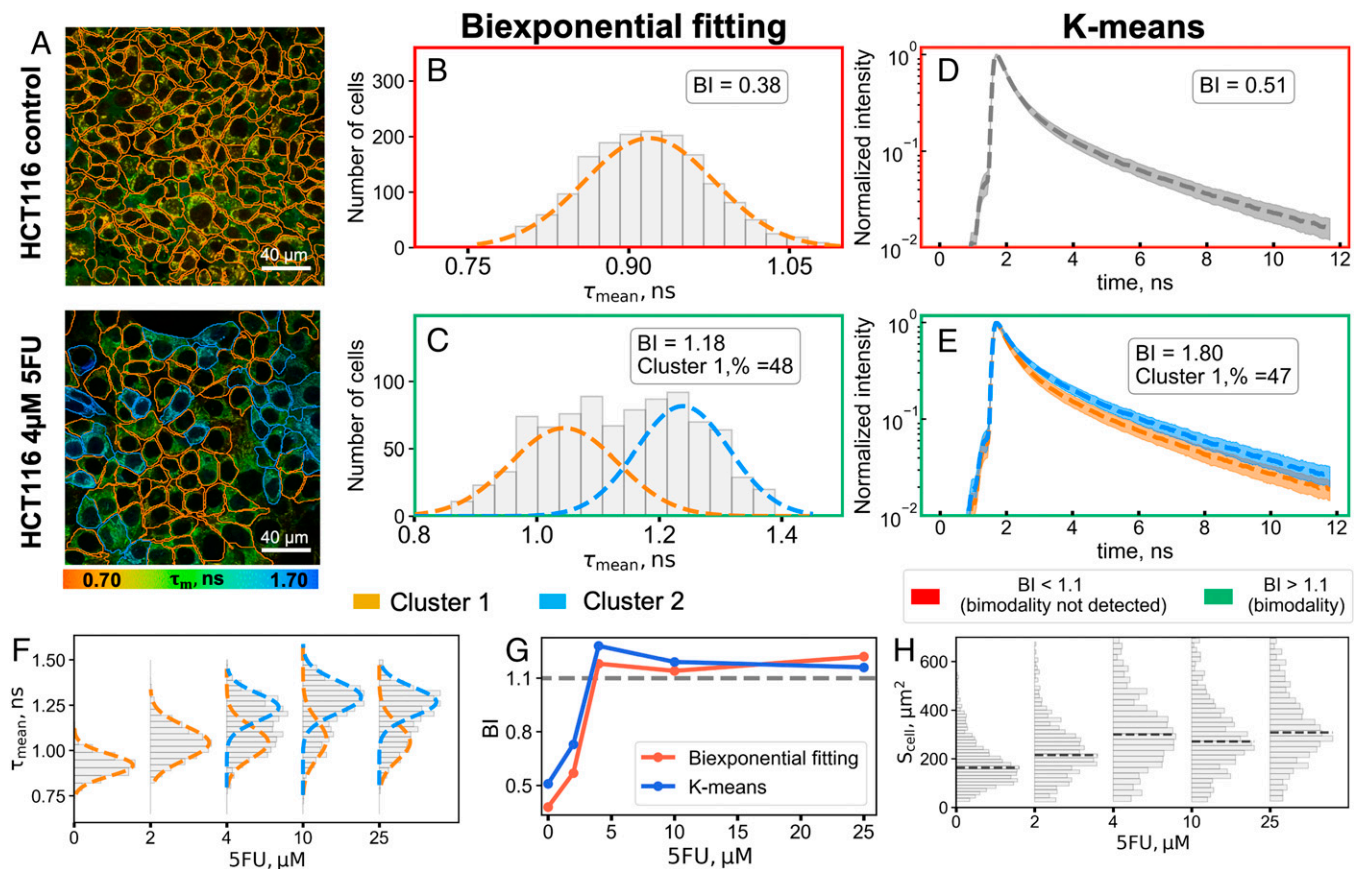


Fig. 4. Experimental assessment of cellular heterogeneity in the human colorectal carcinoma cell line HCT116 treated with 5-FU. (A) Representative FLIM images of NAD(P)H fluorescence of untreated (*Top*) and treated cells (4 μM for 24 h, *Bottom*). Orange and blue contours correspond to two clusters as determined by the K-means algorithm applied for the fluorescence decay curves of the contoured cell. (B and C) The distributions of the mean fluorescence lifetime τ_{mean} for the untreated (B) and treated (C) cells and their fits to two Gaussians. (D and E) The results of K-means clustering for the untreated (D) and treated (E) samples. The two clusters of fluorescence decay curves with centroids are shown by dashed lines. (F) Evolution of the mean fluorescence lifetime distribution with the drug concentration. Orange and blue contours correspond to two clusters as determined in the calculation of the BI. (G) The dependence of BI, calculated from fluorescence lifetime distributions (red) and using K-means clustering (blue), on the drug concentration. (H) The dependence of the cells' area on the 5-FU concentration.

distribution (Fig. 4 B and C) and K-means clustering of fluorescence decay curves (Fig. 4 D and E) for segmented cells.

It is interesting that after the treatment the distribution of the fluorescence lifetime τ_{mean} of single cells evolved in a dose-dependent manner. At the lowest drug dose of 2 μM a small, but statistically significant, shift of the mean fluorescence lifetime was observed, from 0.9 ns to 1.1 ns (t test, $P < 10^{-4}$), and the population of the cells remained metabolically homogenous (Fig. 4F). With the further increase of the dose, separation of the cells into two clusters appeared—with the small and large shifts of the mean fluorescence lifetime of NAD(P)H relative to the control, corresponding to the nonresponsive and the responsive cells, respectively. Increase in the drug dose from 2 μM to 25 μM resulted in an increase of the fraction of metabolically shifted, i.e., responsive, cells up to 75%. It is important to mention that at the dose of 4 μM , close to the half-inhibitory concentration IC_{50} of 3 μM as determined by the MTT assay (see *SI Appendix*, Fig. S7), the portion of responsive cells was $\sim 55\%$, thus confirming that the changes of the mean fluorescence lifetime of NAD(P)H are associated with the decrease of cellular metabolic activity and/or viability. Notably, the BI dependence on the drug concentration (Fig. 4G) corresponded to the viability data of the MTT assay (see *SI Appendix*, Fig. S7).

Automatic segmentation of cells in the FLIM images also allowed for assessment of their morphology. A gradual increase

in the cell area with 5-FU concentration was observed, without however, development of bimodality (Fig. 4H). This indicates that cellular morphology does not correlate with metabolic state of the cells and presents a less reliable metric of the early response to treatment.

As a second example we analyzed metabolic heterogeneity in the cancer cell cultures obtained from the patients' colorectal tumors. It is widely recognized that cell lines do not completely recapitulate their tumor cells of origin as inevitable selection occurs during adaptation of cells to culture conditions and subsequent long-term culturing (33). From this point of view, short-term primary cell cultures represent a more “close-to-patient” model.

For primary cell cultures, FLIM images of NAD(P)H were obtained within 5 to 7 d after isolation of cancer cells from colon tumors and tested for bimodality using three algorithms described above. The data for five patients were processed, four of which showed unimodal and one bimodal distribution of the FDPs. Fig. 5A shows the examples of primary colorectal cancer cells with uniform and heterogeneous metabolism. In the latter case, the K-means algorithm provided the highest BI value as compared to the fitting procedure and phasor plot.

Further, we assessed the response of patients' cultured cells to treatment with 2 or 4 μM of 5-FU. It was observed that for the cell cultures with initially monomodal distribution of the fluorescence lifetime (homogenous metabolism) a shift toward

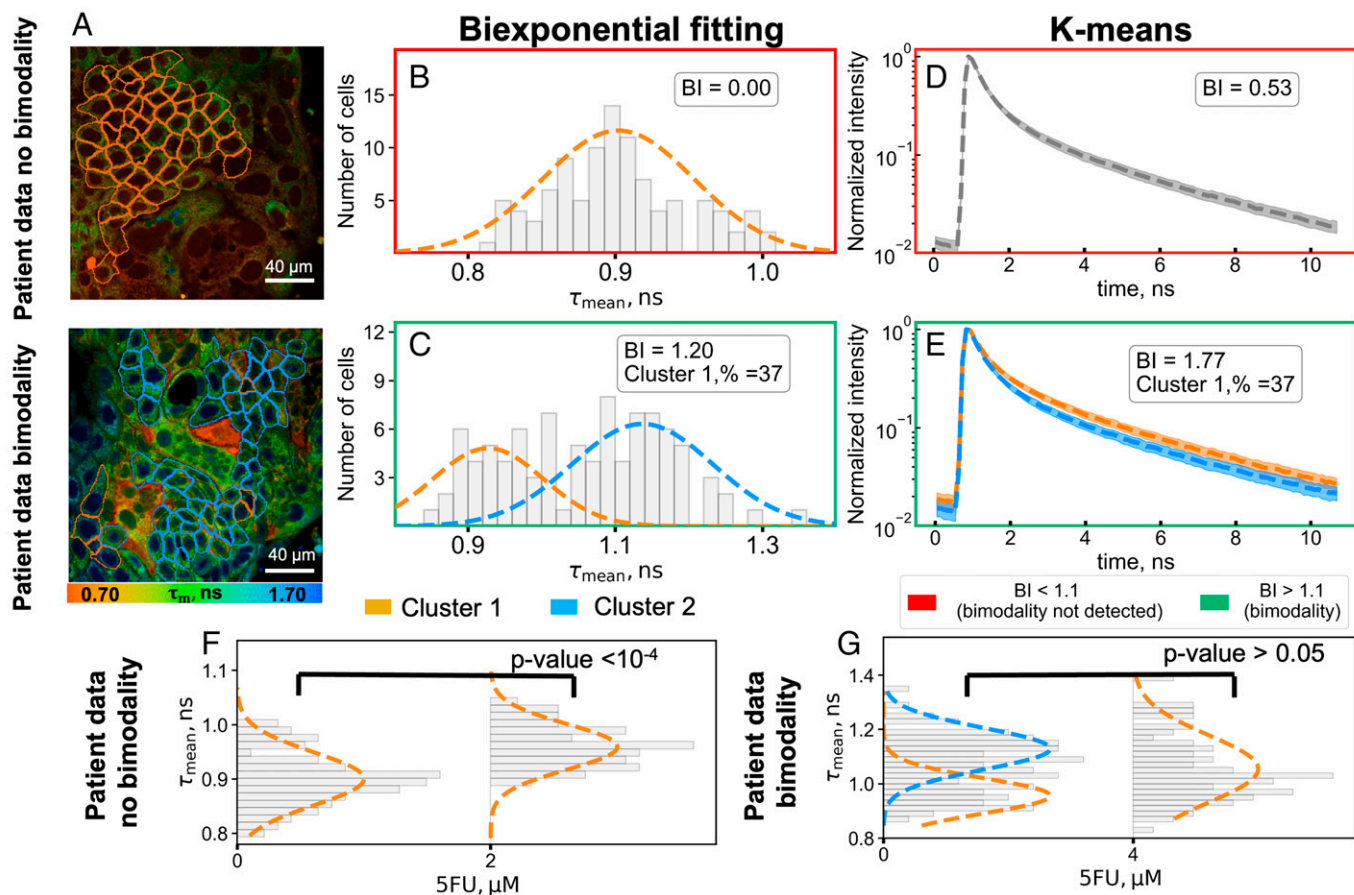


Fig. 5. Experimental assessment of cellular heterogeneity in the primary colon cancer cell cultures. (A) Representative FLIM images of NAD(P)H fluorescence of primary cell cultures exhibiting unimodal (Top) and bimodal (Bottom) metabolism. (B and C) The distributions of the mean fluorescence lifetime for the primary cell cultures exhibiting unimodal (B) and bimodal (C) metabolism and its fits to two Gaussians. (D and E) The results of K-means clustering for the primary cell cultures exhibiting unimodal (D) and bimodal (E) distribution of FDPs. The two clusters of fluorescence decay curves with centroids are shown by dashed lines. (F) Changes of the mean fluorescence lifetime distribution upon treatment with 5-FU for the patient's cells, which exhibited no bimodality. (G) Changes of the mean fluorescence lifetime distribution upon treatment with 5-FU for the patient's cells, which exhibited bimodality. Orange and blue contours in the A and I correspond to two clusters as determined by the K-means algorithm.

higher values took place (t test, $P < 10^{-3}$), similarly to what has been observed for the HCT116 cell line (Fig. 5F; see also *SI Appendix, Table S2*). On the contrary, no statistically significant changes of fluorescence lifetime were observed for the sample, which initially exhibited metabolic heterogeneity (Fig. 5G). These results support the hypothesis that the intrinsic metabolic heterogeneity of cancer cells correlates with the poor response to therapy. In general, observation and quantification of the heterogeneity of cellular metabolism in the patient-derived material has a great clinical importance as it might be relevant for the prognosis of patients and a patient-specific drug screen.

Discussion

Imaging and quantifying tumor heterogeneity is crucially important for assessing tumor progression and tailoring cancer therapy to a specific patient. With molecular characterization and metabolic profiling, significant progress has been made in the recent years in the understanding that a high degree of spatial metabolic heterogeneity exists within tumors. Mapping and quantification of the metabolic heterogeneity at the cellular level is important not only from the point of view of fundamental aspects of carcinogenesis but also for clinical applications.

FLIM microscopy of autofluorescent endogenous metabolic cofactors [NAD(P)H and flavins] allows one to probe cellular metabolism by measuring their fluorescence decay time

(fluorescence lifetime) in live cells and tissues noninvasively and directly observe the contrast between the different structures within the image if they have different metabolic states. Label-free principles of FLIM image acquisition and (sub)cellular resolution make this method a promising instrument to gain insight into metabolic heterogeneity of cancer cells.

Although the metabolic heterogeneity is a commonly recognized feature of tumor cells, the approaches to its quantitative assessment are poorly developed. In this study, we aimed at finding the most sensitive method to assess bimodality in the distribution of FDPs in cellular populations. To quantify the observed bimodality, we used the BI criterion, which gives the natural measure in the case of the presence of the second mode in distribution of the estimated parameter (30). The assessment of the heterogeneity of the FLIM parameters has been previously reported using the weighted heterogeneity (wH) index (34). To the best of our knowledge, this is the only metric to quantify metabolic heterogeneity on the basis of FLIM data for today. A comparison of BI with the wH-index showed that the value of wH-index provides results similar to BI in the heterogeneity evaluation as demonstrated in *SI Appendix, Fig. S8* and discussed in detail in *SI Appendix*. Yet, the BI provides dimensionless estimation on the inherent heterogeneity of a sample, and therefore it can be used to compare heterogeneity assessed by different FDPs and FLIM data analysis methods.

We note that the analysis of fluorescence intensity distribution did not reveal bimodality in the data, thus favoring FLIM as a method for the detection of metabolically distinct cell subpopulations (see *SI Appendix, Fig. S9*).

Using FLIM of NAD(P)H, we tested three approaches to the data processing for bimodality detection: 1) fitting the fluorescence decay to a biexponential decay model, 2) analysis of the FLIM data on the phasor plot, and 3) clustering of the fluorescence decay curves with the K-means algorithm. Additionally, we compared the pixelwise analysis of the whole FLIM image and segmentation of the image into individual cells.

Using numerical simulation, it was demonstrated that the analysis over individual cells always outperforms the analysis over the whole image in terms of metabolic heterogeneity detection (Figs. 2 and 3; see also *SI Appendix, Figs. S2–S4*). Further comparison of three above-mentioned FLIM data analysis methods showed that the K-means clustering correctly identifies the cluster to which the cell belongs in the case of $\Delta\tau_{\text{mean}}$ lower by as much as ~ 50 ps compared to biexponential fitting in the case of predominance of one of the clusters ($\pi = 90\%$; Fig. 3). Hence, this approach was the best for detecting metabolic heterogeneity for clusters of cells with close distributions of FDPs.

The developed FLIM data analysis methods for metabolic heterogeneity assessment were then tested on experimental data. We showed that the extent of heterogeneity (bimodality) can be assessed using the BI, and the fraction of cells in each population can be determined. In the experiments on the HCT116 cancer cell line exposed to 5-FU we found that the chemotherapeutic treatment with the doses $\geq 4 \mu\text{M}$ induced two metabolically distinct subpopulations of cells that had been homogeneous before treatment (Fig. 4). Comparing the results of BI assessments with the MTT assay confirmed that the metabolic changes observed by FLIM of NAD(P)H correlated with cells' response to the treatment. A small shift of the mean fluorescence lifetime of NAD(P)H to a longer value was assigned to nonresponsive cells and a large shift to responsive ones. Overall, the increase of the lifetime can be a result of both inhibition of glycolysis and activation of mitochondrial respiration and presents a nonspecific response to cytotoxic drugs having different mechanisms of action (19, 35, 36). Several reports demonstrate the possibilities of FLIM to reveal heterogeneous drug response on a single-cell level. For example, in our earlier study we showed that the fluorescence lifetime of NAD(P)H is a sensitive parameter for tracking the heterogeneous cellular response to chemotherapy both in cell monolayers and in multicellular tumor spheroids (35). Specifically, metabolic heterogeneity was detected by NAD(P)H fluorescence upon treatment of HeLa (human cervical carcinoma) cells with paclitaxel—a shift to longer lifetimes developed in the more responsive cells (35). Wallrabe et al. identified heterogeneous response of prostate cancer cells AA PCa upon treatment with doxorubicin using NADH-a2%/FAD-a1% ratio (FLIRR) (37). Increased metabolic heterogeneity was shown by Shah et al. in mice with FaDu (hypopharyngeal carcinoma) tumors in vivo and in organoids generated from FaDu tumors after treatment with the cetuximab and cisplatin on the basis of NAD(P)H fluorescence lifetime measurements (38, 39). Although malignant cell lines are expected to be genetically and phenotypically homogeneous cell population, these studies demonstrate that chemotherapy can result in variable cellular responses. This can be associated, for example, with a variability in cell cycle phases in the “nonsynchronized” cell culture or the presence of cancer stem cells, which are intrinsically more resistant to chemotherapy and heterogeneous themselves in terms of differentiation potential.

In vitro drug testing in cultured patient-derived tumor cells is considered a promising approach for individualization of

treatment; however, there is still a lack of “ready-to-use” assays (40, 41). One of the issues in this methodology is the absence of reliable, quantitative metrics of cell response, which could be measured on relatively small number of isolated cells and would take into account cellular-level heterogeneity. This motivated us to test the suggested algorithms on the short-term cell cultures generated from patient tumors. We found that, in contrast to the established cell line, primary cells can be intrinsically heterogeneous in their metabolism. For the patient-derived cells, cellular metabolic heterogeneity detected before treatment yielded poor response to 5-FU. In general, the patient-derived cells were less sensitive to chemotherapy and displayed less-pronounced metabolic changes, resembling those induced by the low dose of the drug in HCT116 cells. Previously, Sharick et al. observed cellular heterogeneity of drug response in breast cancer and pancreatic cancer patient-derived organoids. Heterogeneous metabolic response in organoids treated with the same drugs as the patient's prescribed regimen agreed with a poor outcome for patients (42). Recently, Gillette et al. showed that a single-cell metabolic heterogeneity of neuroendocrine patient-derived tumor organoids is consistent with the overall treatment response: Highly heterogeneous organoids were nonresponsive to all the treatments (43), which agree with our results.

The proposed approach based on the BI calculation using FLIM of NAD(P)H and the K-means method in combination with automatic cell segmentation has a high potential for the development of high-throughput screening platforms for drug sensitivity assessments. The limitation of our approach is that only two groups of cells are considered (i.e., bimodal distribution). The introduced BI could be modified to account for the presence of multiple groups at the same time. However, we did not observe more than two groups in our data, and a much larger number of cells is needed to be able to distinguish more than two groups if they are present in the population. While our investigation was focused on just one FDP, τ_{mean} , the same approach can be used for other parameters like the relative contributions of free or bound NAD(P)H, or fluorescence lifetime of the bound form of NAD(P)H. In general, the underlying reasons for metabolic variability, both initial and developed after treatment, have yet to be clarified, and this will be the focus of our future research. Further investigations of our group will also include more samples and a long-term follow-up of the patients and will aim to find the associations between the baseline heterogeneity of patient-derived cancer cells and treatment outcome. We also note (*SI Appendix, Fig. S10*) that we are developing more advanced spectroscopic imaging methods based on quantum optics, which can potentially improve the accuracy of FLIM measurements while maintaining their viability of cell culture under study. In summary, the results obtained in this work provide a methodological basis for a sensitive and quantitative analysis of bimodality of FDPs of cells and pave the way for a more precise detection and quantification of cellular metabolic heterogeneity using FLIM. Nowadays, the choice of chemotherapy protocol for patients is determined on the basis of histological diagnosis, while individual properties of a patient's tumor are not taken into account, which limits the efficacy of treatment. This fact stimulates the search of the early predictors of chemotherapy effectiveness. We believe that identification and accurate assessment of cellular metabolic heterogeneity of patients' tumors with the use of suggested algorithms can become a valuable approach to develop improved, individualized treatment regimens.

Materials and Methods

FLIM Data Modeling. Each cell was simulated as a square of 45×45 with a nucleus of 20×20 pixels on the image of 512×512 pixels. After that, a

fluorescence decay curve was generated for each pixel based on the biexponential decay law, and the decay parameters a_1, a_2, τ_1, τ_2 were all normally distributed with relative deviation of 15% from the average within each cell. Then, the decay curves were convolved with the IRF modeled as a Gaussian function with $\sigma_{\text{IRF}} = 100$ ps. After that, a Poisson noise was added to each decay curve. Two clusters of cells were modeled by setting two sets of mean FDPs for each cluster.

The values of photophysical parameters of fluorescence decay curves were selected to match the experimentally observed data of NAD(P)H FLIM. The corresponding parameters were selected for the different cell compartments. The FDPs of cell cytoplasm setted as follows: $a_1^{(\text{cytoplasm})} = 7, a_2^{(\text{cytoplasm})} = 2.6, \tau_1^{(\text{cytoplasm})} = 400$ ps, $\tau_2^{(\text{cytoplasm})} = 2,700$ ps; the typical nuclei FDPs were $a_1^{(\text{nuclei})} = 3.5, a_2^{(\text{nuclei})} = 1, \tau_1^{(\text{nuclei})} = 400$ ps, $\tau_2^{(\text{nuclei})} = 2,200$ ps, and for the background $a_1^{(\text{background})} = 0.5, a_2^{(\text{background})} = 0.5, \tau_1^{(\text{background})} = 600$ ps, $\tau_2^{(\text{background})} = 3,000$ ps. Taking the number of time bins as 500 (each corresponding to 40 ps), these parameters correspond to the average of 100 photons over the fluorescence decay (and 10 photons in maximum) for the cell, 35 photons over the fluorescence decay (and 5 photons in maximum) for the nuclei region, and 15 photons over the fluorescence decay (1 photon in maximum) for the background per pixel. The representative fluorescence decay curves from cell cytoplasm, nuclei, and background are presented in *SI Appendix, Fig S1*.

To model the heterogeneity in subpopulation, values of cytoplasm FDPs of 50, 70, or 90% of cells were adjusted using the a_1/a_2 ratio in the way that specific $\Delta\tau_m = \tau_m^{(2)} - \tau_m^{(1)}$ was achieved, while the number of photons under the fluorescence decay curves on average was fixed to 100. Exemplary parameters set for each subsample are presented in *SI Appendix, Table S3*.

After the modeling of the FDPs distribution, 50 cells were placed on the image of 512×512 pixels, and for each numerical experiment 10 images were considered. Two types of analysis were performed to obtain distribution of FDPs. In the first case, FDPs were obtained by fitting the decay curves in binned pixels (binning = 3, corresponding to the window of 9×9 pixels). In the second case, fluorescence decay curves were averaged for all the pixels inside each cell. The obtained fluorescence decay curves were analyzed using biexponential fitting with respect to the Gaussian IRF, phasor approach, and the K-means clustering procedure. The amplitudes (a_1, a_2) and characteristic lifetimes (τ_1, τ_2) estimated using biexponential fitting procedure were used to calculate the mean fluorescence lifetime as $\tau_m = (\tau_1 \cdot a_1 + \tau_2 \cdot a_2) / (a_1 + a_2)$.

BI Calculation for Average Fluorescence Lifetime. The BI for distributions of average fluorescence lifetime was calculated as follows. Each obtained τ_m sample was fitted using an expectation maximization algorithm that fit the distribution of $\rho(\tau_m)$ to the weighted mixture of two normal distributions $N(\tau_m, \sigma)$ with different centers $\tau_m^{(1)}$ and $\tau_m^{(2)}$ and different SDs $\sigma^{(1)}, \sigma^{(2)}$, i.e.,

$$\rho(\tau_m) = \pi \cdot N(\tau_m^{(1)}, \sigma^{(1)}) + (1 - \pi) \cdot N(\tau_m^{(2)}, \sigma^{(2)}) \quad [1]$$

After that, the BI was calculated as

$$BI = \sqrt{\pi(1-\pi)} \cdot \frac{|\tau_{\text{mean}}^{(2)} - \tau_{\text{mean}}^{(1)}|}{\sqrt{\sigma^{(1)}\sigma^{(2)}}} \quad [2]$$

where $\pi = \frac{N_1}{N_1+N_2}$.

BI Calculation for Phasor Parameters. The phasor analysis of fluorescence decay curves was conducted according to ref. 24. Only the time bins with non-zero data were used to calculate C and S phasor parameters. No additional IRF corrections were applied to the data before the phasor analysis.

Similarly to the calculation of BI for distribution of average fluorescence lifetimes, the BI was assessed in a two-step manner. First, the distributions of phasor parameters were fitted using expectation maximization algorithm to mixture of two normal distributions:

$$\rho(c, s) = \pi \cdot N(\bar{\mu}^{(1)}, \hat{\sigma}^{(1)}) + (1 - \pi) \cdot N(\bar{\mu}^{(2)}, \hat{\sigma}^{(2)}), \quad [3]$$

where $N(\bar{\mu}^{(i)}, \hat{\sigma}^{(i)})$ is the density function of bivariate normal distribution.

After obtaining the values of centers of two Gaussians $[(\mu_c^{(1)}, \mu_s^{(1)})$ and $(\mu_c^{(2)}, \mu_s^{(2)})$] and their SDs $[\sigma^{(1)}$ and $\sigma^{(2)}]$, the BI was calculated as

$$BI_{c,s} = \sqrt{\pi(1-\pi)} \cdot \frac{\|\mu^{(1)} - \mu^{(2)}\|_{L_2}}{\sqrt{\sigma^{(1)}\sigma^{(2)}}} = \sqrt{\pi(1-\pi)} \cdot \frac{\sqrt{(\mu_c^{(1)} - \mu_c^{(2)})^2 + (\mu_s^{(1)} - \mu_s^{(2)})^2}}{\sqrt{\sigma^{(1)}\sigma^{(2)}}} \quad [4]$$

where $(\sigma^{(i)})^2 = (\sigma_c^{(i)})^2 + (\sigma_s^{(i)})^2, i = 1, 2$.

K-Means Clustering of Fluorescence Decay Curves. The fluorescence decay curves obtained for a given numerical experiment (i.e., for fixed π and $\Delta\tau_m$ values) were preliminary normalized to the $[0,1]$ range to avoid the dependency of clustering results on the fluorescence intensity. Then, each normalized fluorescence decay curve was exponentially transformed to reduce the difference between intensities in different time bins. After that, each fluorescence decay curve was treated as object with a feature-vector $\{I(t_1), I(t_2), \dots, I(t_{500})\}$, where $I(t_i)$ corresponds to the transformed intensity in the time bin t_i . After that, the K-means clustering algorithm with two clusters was applied to the object-feature matrix composed of preprocessed fluorescence decay curves. Using the obtained cluster labels for each decay curve and cluster centroids, i.e., fluorescence decay curves averaged within each cluster, the BI was calculated as described further.

BI Calculation for Clustered Fluorescence Decay Curves. After the K-means clustering, two sets of fluorescence decay curves were obtained, and for each cluster the centroid fluorescence decay curve (centroid) was calculated. Calculation of intracluster deviations $[\sigma^{(1)}$ and $\sigma^{(2)}]$ was performed as follows:

$$\sigma^{(1)} = \sqrt{\frac{\sum_{j \in \text{Cluster 1}} \|y_j - y^{(1)}\|_{L_2}^2}{N_1}}, \sigma^{(2)} = \sqrt{\frac{\sum_{j \in \text{Cluster 2}} \|y_j - y^{(2)}\|_{L_2}^2}{N_2}}, \quad [5]$$

where the summation is performed for all fluorescence decay curves y_j attributed either to the first or to the second cluster with centroids $y^{(1)}, y^{(2)}$, and corresponding numbers of fluorescence decay curves N_1 and N_2 . After that, BI was calculated using the L_2 distance between centroids $y^{(1)}, y^{(2)}$ and estimated SDs $\sigma^{(1)}, \sigma^{(2)}$:

$$BI_{Km} = \sqrt{\pi(1-\pi)} \frac{\|y^{(1)} - y^{(2)}\|_{L_2}}{\sqrt{\sigma^{(1)}\sigma^{(2)}}} \quad [6]$$

where π was calculated using the fraction of fluorescence decay curves attributed to the cluster with index "1", i.e., $\pi = \frac{N_1}{N_1+N_2}$.

All simulation and data analysis were performed using custom-build Python 3.7 scripts with the use of Numpy, Scipy, Scikit-Learn Matplotlib, Pandas and LmFit modules. The implementations of K-means and expectation maximization algorithms from the Scikit-learn module were used in the calculations (44).

Cluster Performance Evaluation. To characterize the predictive capabilities of the three methods in the assessment of cellular heterogeneity, the metrics called precision was computed as follows:

$$\text{Precision} = \frac{TP}{TP + FN} \cdot 100\%, \quad [7]$$

where TP is the number of cells correctly attributed to Cluster 1 (true positive) and FN is the number of cells from Cluster 1 (with lower fluorescence lifetime) which were incorrectly referred to Cluster 2 (false negative).

Cell Segmentation Algorithm. In this work we implemented automatic segmentation of the human colon adenocarcinoma line HCT116 cells and cancer cell cultures obtained from the patients' colorectal tumors. We used a hybrid approach that utilizes the combination of the deep learning routines, namely, the U-Net neural network, which is widely used for binary segmentation of medical images (31, 45, 46), combined with computer vision algorithms and heuristics for object segmentation. The implemented algorithm is schematically shown in Fig. 6.

First, the intensity images were normalized to the $[-0.5, 0.5]$ range to match the inputs of the U-net neural network. Then, the preprocessed images served as an input of the multiple U-nets, which predicted cells' borders, inner regions of cells, and cells' nuclei, i.e., each U-net for a given image predicted a map of probabilities for pixels to belong to a cell's border, inner region (cytoplasm or nuclei), or nucleus. The U-nets were preliminary trained on the manually segmented images for correct probability mask prediction. The obtained probability masks were binarized and postprocessed using morphological operations, and the probability masks of cells' nuclei were used to compute the nuclei centroids. The processed binary masks and positions of the nuclei centroids were used to calculate distance maps from the nuclei centers to the cells' borders. The obtained distance maps were further subject to the watershed algorithm, which returned the final masks.

As for the patient-derived materials exhibited artifacts related to irregular cell morphology and uneven sectioning, only the cells inside manually specified region were segmented, while the images of the HCT116 cells were processed as is. The details on the U-nets training, morphological operations, thresholding and other procedures are given in *SI Appendix*.

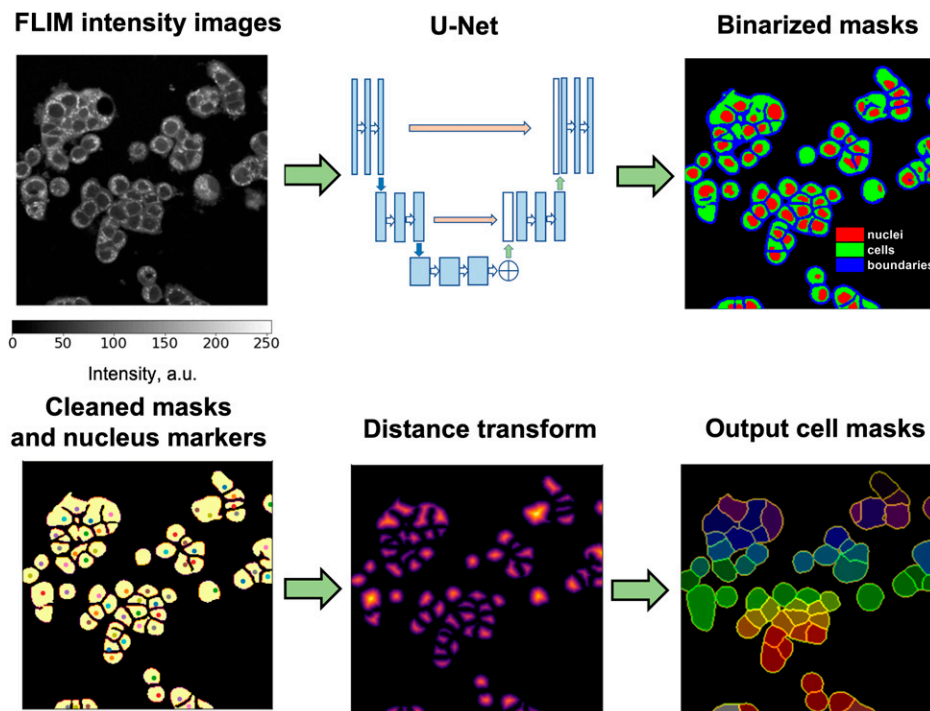


Fig. 6. Schematic of the U-Net model-based algorithm for cell segmentation in the FLIM data.

FLIM Measurements. FLIM measurements on live cultured cells were performed using an LSM 880 (Carl Zeiss) laser-scanning microscope equipped with a FLIM module Simple Tau 152 TCSPC (Becker & Hickl GmbH). Two-photon fluorescence of NAD(P)H was excited with a femtosecond Ti:Sa laser (repetition rate 80 MHz, pulse duration 140 fs) at a wavelength of 750 nm and registered in the range 455 to 500 nm. A water immersion objective (C-Apochromat 40x/1.2 W Corr, Zeiss, Inc.) was used for image acquisition. The average power applied to the samples was ~ 6 mW. Image collection time was 60 s. During image acquisition, the cells were maintained at 37 °C and 5% CO₂.

Cell Cultures. The human colorectal carcinoma cell line HCT116 was routinely grown in Dulbecco's modified Eagle's medium (DMEM) (PanEko) supplemented with 10% fetal bovine serum (HyClone), 2 mM glutamine, 10 mg/mL penicillin, and 10 mg/mL streptomycin. The cells were incubated at 37 °C, 5% CO₂, and 80% relative humidity and passaged three times a week.

For fluorescence microscopy the cells were seeded (1×10^5 in 2 mL) in glass-bottomed 35 mm FluoroDishes and incubated 48 h (37 °C, 5% CO₂). Then, the cells were washed with phosphate-buffered saline solution and placed in DMEM life medium without phenol red. The monolayer cells were incubated with 5-FU (Veropharm) at the concentrations 2, 4, 10, and 25 μ M for 24 h. Untreated cells served as a control. In total, five FLIM images were obtained both for the control and treated samples from randomly selected fields of view.

Surgical samples of patients' colon tumors were provided by the Volga District Medical Center (Nizhny Novgorod) in accordance with protocols approved by the local ethical committee. All the patients included in the study had a histological verification of colorectal cancer and had not been pre-treated with radiotherapy or chemotherapy. Primary cell cultures were isolated from tumors using the protocol described in ref. 47. After isolation, the cells were seeded in 96-well black/clear plates (Falcon; Corning Incorporated)

precoated with collagen I (Gibco), ~ 5 to 10×10^3 cells in 200 μ L DMEM per well. The medium was changed after 3 d. FLIM was performed in 5 to 7 d after seeding, upon cells attachment, which was controlled with light microscopy. In total, 10 FLIM images were acquired for each sample. Clinicopathological data of cancer patients are present in *SI Appendix, Table S4*.

Data Availability. All study data are included in the article and/or *SI Appendix*.

ACKNOWLEDGMENTS. Development of the algorithms for FLIM data processing was supported by the Russian Science Foundation (project 20-65-46018). The work with primary cell cultures was supported by the Ministry of Health of the Russian Federation as part of the Government assignment (Privolzhskiy Research Medical University (PRMU), reg. #AAAA-A20-120022590098-0, M.V.S. Principal Investigator). We thank Irina Druzhkova, Liubov Shimolina, Vadim Elagin, and Alena Gavrina (PRMU) for their kind assistance with biological studies and Prof. Vladimir E. Zagainov (Volga District Medical Center) for support of the clinical research. V.V.Y. acknowledges partial support of the NSF (DBI-1455671, ECCS-1509268, and CMMI-1826078), the Air Force Office of Scientific Research (AFOSR; FA9550-15-1-0517, FA9550-20-1-0366, and FA9550-20-1-0367), Army Medical Research Grant (W81XWH2010777), the NIH (1R01GM127696-01 and 1R21GM142107-01), and the Cancer Prevention and Research Institute of Texas (RP180588). M.O.S. acknowledges support from the AFOSR (FA9550-20-1-0366 and FA9550-20-1-0367), the Office of Naval Research (N00014-20-1-2184), the Robert A. Welch Foundation (Grant A-1261), and the NSF (PHY-2013771). The work of E.A.S., A.V.G., B.P.Y., and G.S.B. was performed under the Development program of the Interdisciplinary Scientific and Educational School of Lomonosov Moscow State University "Photonic and Quantum technologies. Digital medicine." The work of A.V.G. on the data analysis was supported by the Foundation for the Advancement of Theoretical Physics and Mathematics "Basis" scholarship for Master students (scholarship no. 20-2-9-2-1).

1. A. Marusyk, K. Polyak, Tumor heterogeneity: Causes and consequences. *Biochim. Biophys. Acta* **1805**, 105–117 (2010).
2. T. A. Denison, Y. H. Bae, Tumor heterogeneity and its implication for drug delivery. *J. Control. Release* **164**, 187–191 (2012).
3. M. Robertson-Tessi, R. J. Gillies, R. A. Gatenby, A. R. A. Anderson, Impact of metabolic heterogeneity on tumor growth, invasion, and treatment outcomes. *Cancer Res.* **75**, 1567–1579 (2015).
4. J. Kim, R. J. DeBerardinis, Mechanisms and implications of metabolic heterogeneity in cancer. *Cell Metab.* **30**, 434–446 (2019).
5. D. Jia, J. H. Park, K. H. Jung, H. Levine, B. A. Kaipparettu, Elucidating the metabolic plasticity of cancer: Mitochondrial reprogramming and hybrid metabolic states. *Cells* **7**, 21 (2018).
6. J. Zheng, Energy metabolism of cancer: Glycolysis versus oxidative phosphorylation (Review). *Oncol. Lett.* **4**, 1151–1157 (2012).
7. M. V. Berridge, P. M. Herst, A. S. Tan, Metabolic flexibility and cell hierarchy in metastatic cancer. *Mitochondrion* **10**, 584–588 (2010).
8. R. Diaz-Ruiz, M. Rigoulet, A. Devin, The Warburg and Crabtree effects: On the origin of cancer cell energy metabolism and of yeast glucose repression. *Biochim. Biophys. Acta* **1807**, 568–576 (2011).
9. V. R. Fantin, J. St-Pierre, P. Leder, Attenuation of LDH-A expression uncovers a link between glycolysis, mitochondrial physiology, and tumor maintenance. *Cancer Cell* **9**, 425–434 (2006).
10. J. R. Lakowicz, H. Szymanski, K. Nowaczyk, M. L. Johnson, Fluorescence lifetime imaging of free and protein-bound NADH. *Proc. Natl. Acad. Sci. U.S.A.* **89**, 1271–1275 (1992).

11. M. C. Skala *et al.*, In vivo multiphoton microscopy of NADH and FAD redox states, fluorescence lifetimes, and cellular morphology in precancerous epithelia. *Proc. Natl. Acad. Sci. U.S.A.* **104**, 19494–19499 (2007).
12. A. T. Shah *et al.*, Optical metabolic imaging of treatment response in human head and neck squamous cell carcinoma. *PLoS One* **9**, e90746 (2014).
13. J. L. Qu *et al.*, Gastric cancer exosomes promote tumour cell proliferation through PI3K/Akt and MAPK/ERK activation. *Dig. Liver Dis.* **41**, 875–880 (2009).
14. X. Liu *et al.*, Fast fluorescence lifetime imaging techniques: A review on challenge and development. *J. Innov. Opt. Health Sci.* **12**, 1930003 (2019).
15. J. M. Jabbour *et al.*, Fluorescence lifetime imaging and reflectance confocal microscopy for multiscale imaging of oral precancer. *J. Biomed. Opt.* **18**, 046012 (2013).
16. D. K. Bird *et al.*, Metabolic mapping of MCF10A human breast cells via multiphoton fluorescence lifetime imaging of the coenzyme NADH. *Cancer Res.* **65**, 8766–8773 (2005).
17. J. McGinty *et al.*, Wide-field fluorescence lifetime imaging of cancer. *Biomed. Opt. Express* **1**, 627–640 (2010).
18. A. Cong *et al.*, Two-photon fluorescence lifetime imaging of intrinsic NADH in three-dimensional tumor models. *Cytometry A* **95**, 80–92 (2019).
19. M. V. Shirmanova *et al.*, Chemotherapy with cisplatin: Insights into intracellular pH and metabolic landscape of cancer cells in vitro and in vivo. *Sci. Rep.* **7**, 8911 (2017).
20. M. M. Lukina *et al.*, Interrogation of tumor metabolism in tissue samples ex vivo using fluorescence lifetime imaging of NAD(P)H. *Methods Appl. Fluoresc.* **8**, 014002 (2019).
21. J. T. Sharick *et al.*, Cellular metabolic heterogeneity in vivo is recapitulated in tumor organoids. *Neoplasia* **21**, 615–626 (2019).
22. T. M. Heaster, B. A. Landman, M. C. Skala, Quantitative spatial analysis of metabolic heterogeneity across *in vivo* and *in vitro* tumor models. *Front. Oncol.* **9**, 1144 (2019).
23. A. J. Walsh *et al.*, Quantitative optical imaging of primary tumor organoid metabolism predicts drug response in breast cancer. *Cancer Res.* **74**, 5184–5194 (2014).
24. M. A. Digman, V. R. Caiolfa, M. Zamai, E. Gratton, The phasor approach to fluorescence lifetime imaging analysis. *Biophys. J.* **94**, L14–L16 (2008).
25. C. Stringari *et al.*, Phasor approach to fluorescence lifetime microscopy distinguishes different metabolic states of germ cells in a live tissue. *Proc. Natl. Acad. Sci. U.S.A.* **108**, 13582–13587 (2011).
26. R. Brodewolf *et al.*, Faster, sharper, more precise: Automated Cluster-FLIM in preclinical testing directly identifies the intracellular fate of theranostics in live cells and tissue. *Theranostics* **10**, 6322–6336 (2020).
27. B. Kaye, P. J. Foster, T. Y. Yoo, D. J. Needleman, Developing and testing a Bayesian analysis of fluorescence lifetime measurements. *PLoS One* **12**, e0169337 (2017).
28. S. Wang, J. V. Chacko, A. K. Sagar, K. W. Elicieiri, M. Yuan, Nonparametric empirical Bayesian framework for fluorescence-lifetime imaging microscopy. *Biomed. Opt. Express* **10**, 5497–5517 (2019).
29. J. T. Smith *et al.*, Fast fit-free analysis of fluorescence lifetime imaging via deep learning. *Proc. Natl. Acad. Sci. U.S.A.* **116**, 24019–24030 (2019).
30. J. Wang, S. Wen, W. F. Symmans, L. Pusztai, K. R. Coombes, The bimodality index: A criterion for discovering and ranking bimodal signatures from cancer gene expression profiling data. *Cancer Inform.* **7**, 199–216 (2009).
31. O. Ronneberger, P. Fischer, T. Brox, "U-Net: Convolutional networks for biomedical image segmentation" in *Medical Image Computing and Computer-Assisted Intervention – MICCAI 2015. MICCAI 2015. Lecture Notes in Computer Science*, N. Navab, J. Hornegger, W. Wells, A. Frangi, Eds. (Springer Verlag, 2015), vol. 9351, pp. 234–241.
32. E. H. Schreuders *et al.*, Colorectal cancer screening: A global overview of existing programmes. *Gut* **64**, 1637–1649 (2015).
33. J. P. Gillet, S. Varma, M. M. Gottesman, The clinical relevance of cancer cell lines. *J. Natl. Cancer Inst.* **105**, 452–458 (2013).
34. A. J. Walsh, M. C. Skala, Optical metabolic imaging quantifies heterogeneous cell populations. *Biomed. Opt. Express* **6**, 559–573 (2015).
35. M. M. Lukina *et al.*, Metabolic cofactors NAD(P)H and FAD as potential indicators of cancer cell response to chemotherapy with paclitaxel. *Biochim. Biophys. Acta, Gen. Subj.* **1862**, 1693–1700 (2018).
36. M. M. Lukina *et al.*, In vivo metabolic and SHG imaging for monitoring of tumor response to chemotherapy. *Cytometry A* **95**, 47–55 (2019).
37. H. Wallrabe *et al.*, Segmented cell analyses to measure redox states of autofluorescent NAD(P)H, FAD & Trp in cancer cells by FLIM. *Sci. Rep.* **8**, 79 (2018).
38. A. T. Shah, K. E. Diggins, A. J. Walsh, J. M. Irish, M. C. Skala, In vivo autofluorescence imaging of tumor heterogeneity in response to treatment. *Neoplasia* **17**, 862–870 (2015).
39. A. T. Shah, T. M. Heaster, M. C. Skala, Metabolic imaging of head and neck cancer organoids. *PLoS One* **12**, e0170415 (2017).
40. D. P. Kodack *et al.*, Primary patient-derived cancer cells and their potential for personalized cancer patient care. *Cell Rep.* **21**, 3298–3309 (2017).
41. A. A. Popova, P. A. Levkin, Precision medicine in oncology: In vitro drug sensitivity and resistance test (DSRT) for selection of personalized anticancer therapy. *Adv. Ther.* **3**, 1900100 (2020).
42. J. T. Sharick *et al.*, Metabolic heterogeneity in patient tumor-derived organoids by primary site and drug treatment. *Front. Oncol.* **10**, 553 (2020).
43. A. A. Gillette *et al.*, Autofluorescence imaging of treatment response in neuroendocrine tumor organoids. *Cancers (Basel)* **13**, 1873 (2021).
44. F. Pedregosa *et al.*, Scikit-learn: Machine learning in Python. *J. Mach. Learn. Res.* **12**, 2825–2830 (2011).
45. T. Falk *et al.*, U-Net: Deep learning for cell counting, detection, and morphometry. *Nat. Methods* **16**, 67–70 (2019).
46. C. McQuin *et al.*, CellProfiler 3.0: Next-generation image processing for biology. *PLoS Biol.* **16**, e2005970 (2018).
47. I. Druzhkova *et al.*, E-Cadherin in colorectal cancer: Relation to chemosensitivity. *Clin. Colorectal Cancer* **18**, e74–e86 (2019).